

Physics-informed machine learning of reduced-order model

Wenqian Chen^a, Qian Wang^{b,*}, Jan S. Hesthaven^b, Chuhua Zhang^a

^a*Department of Fluid Machinery and Engineering, School of Energy and Power Engineering, Xi'an Jiaotong University, Xi'an, Shaanxi, People's Republic of China*

^b*Chair of Computational Mathematics and Simulation Science, École polytechnique fédérale de Lausanne, 1015 Lausanne, Switzerland*

Abstract

A physics-informed machine learning framework is developed for the reduced-order modeling of parametrized steady-state partial differential equations (PDEs). In the offline stage, a reduced-order model is constructed by projecting the high-fidelity numerical model onto a reduced space, spanned by a set of basis functions that represent the main dynamics of the full-order model. A physics informed neural network (PINN), which approximates the mapping from the parameters to the reduced coefficients, is trained by minimizing the loss function as a sum of the residual of the reduced-order model and the matching error with the projection of high-fidelity snapshots onto the reduced space. In the online stage, given a new parameter location, the reduced coefficients are predicted by the physics-informed neural network. Numerical results demonstrate that the PINN can provide fast and accurate solutions to nonlinear problems.

Keywords: physics-informed machine learning, reduced-order modeling, nonlinear PDE

1. Introduction

Why we need reduced-order modeling.

Intrusive reduced-order model. POD-G is a classical choice. Pros and cons.

Intrusive reduced-order model. POD-NN is a recently developed one. Pros and cons. Especially the need of large amount of data for training.

We propose to use physics-informed machine learning to improve the reduced-order modeling by taking advantage of both physics and data. Then explain the idea.

The advantage of PINN over POD-G and POD-NN. Numerical results demonstrate the advantages.

The remainder of this paper is organized as follows.

2. Projection-based reduced basis method

Consider a nonlinear dynamic system governed by partial differential equations(PDEs):

$$\begin{aligned}\mathcal{N}(\phi(\mathbf{x}); \boldsymbol{\mu}) &= 0, & \mathbf{x} &\in \Omega(\boldsymbol{\mu}) \\ \mathcal{B}(\phi(\mathbf{x}); \boldsymbol{\mu}) &= 0, & \mathbf{x} &\in \partial\Omega(\boldsymbol{\mu})\end{aligned}\tag{1}$$

where \mathcal{N} is a general nonlinear differential operator, $\phi(\mathbf{x})$ are field variables to be solved on Cartesian coordinates \mathbf{x} . \mathcal{B} are operators defining boundary conditions for the boundary $\partial\Omega$ of the physical

*Corresponding author.

Email addresses: wenqianchen2016@gmail.com (Wenqian Chen), qian.wang@epfl.ch (Qian Wang), Jan.Hesthaven@epfl.ch (Jan S. Hesthaven), chzhang@mail.xjtu.edu.cn (Chuhua Zhang)

domain Ω . $\boldsymbol{\mu} \in \mathcal{P}$ are specific parameters characterizing the nonlinear dynamic system as well as the physical domain Ω , where \mathcal{P} is the parameter space.

As is always the case for reduced-order methods, a dynamic system is approximated by finding the its projection in a space spanned by a few well-chosen basis vectors. These basis are generated from a suitable linear combination of some precomputed high-fidelity approximations, termed as snapshots. To ensure the compatibility among snapshots, the variable physical domain has to be addressed. To this end, the variable physical domains will be mapped into a fixed computational domain with the same collation of degree of freedoms. This can be implemented by a invertible problem-dependent mapping $\mathcal{X} : \mathbf{x} \in \Omega(\boldsymbol{\mu}) \rightarrow \boldsymbol{\xi} \in \tilde{\Omega}$, which reads

$$\boldsymbol{\xi} = \mathcal{X}(\mathbf{x}; \boldsymbol{\mu}), \quad (2)$$

and thus the governing equations (1) are recast as follows:

$$\begin{aligned} \mathcal{N}(\phi(\mathcal{X}^{-1}(\boldsymbol{\xi}; \boldsymbol{\mu})); \boldsymbol{\mu}) &:= \tilde{\mathcal{N}}(\phi(\boldsymbol{\xi}); \boldsymbol{\mu}) = 0, & \boldsymbol{\xi} \in \tilde{\Omega} \\ \mathcal{B}(\phi(\mathcal{X}^{-1}(\boldsymbol{\xi}; \boldsymbol{\mu})); \boldsymbol{\mu}) &:= \tilde{\mathcal{B}}(\phi(\boldsymbol{\xi}); \boldsymbol{\mu}) = 0, & \boldsymbol{\xi} \in \partial\tilde{\Omega} \end{aligned} \quad (3)$$

where $\tilde{\Omega}$ is the computational domain, $\tilde{\mathcal{B}}$ and $\tilde{\mathcal{N}}$ are derived operators in computational space resulting from transformation Eq. (2).

2.1. Full-order model

To simulate the nonlinear dynamic system in Eqs. (3), the including spatial derivatives are always first discretized by a suitable high-fidelity (HF) method (such as the pseudospectral method, spectral difference method, etc.). To achieve a satisfactory numerical accuracy, a fine mesh is employed with a large number of degrees of freedom (DOFs), generally including N interior DOFs and N_B boundary DOFs. Finally, the resulting discretized equations for Eqs. (3) are solved with a suitable explicit/implicit solver.

Here we denote the discrete solutions of Eq (3) in vector form $\boldsymbol{\phi}_h \in \mathbf{R}^N$ and $\boldsymbol{\phi}_h^B \in \mathbf{R}^{N_B}$ for parameter $\boldsymbol{\mu} \in \mathcal{P}$. Given a suitable HF method, we have the governing Eq. (3) in discrete form

$$\mathbf{L}_{\tilde{\mathcal{N}}} \boldsymbol{\phi}_h + g_{\tilde{\mathcal{N}}}(\boldsymbol{\phi}_h, \boldsymbol{\phi}_h^B) + \mathbf{C}_{\tilde{\mathcal{N}}} = 0 \quad (4)$$

$$\mathbf{L}_{\tilde{\mathcal{B}}} \boldsymbol{\phi}_h + \mathbf{L}_{\tilde{\mathcal{B}}}^B \boldsymbol{\phi}_h^B + \mathbf{C}_{\tilde{\mathcal{B}}} = 0 \quad (5)$$

where $\mathbf{L}_{\tilde{\mathcal{N}}} \in \mathbf{R}^{N \times N}$, $\mathbf{L}_{\tilde{\mathcal{B}}} \in \mathbf{R}^{N_B \times N}$ and $\mathbf{L}_{\tilde{\mathcal{B}}}^B \in \mathbf{R}^{N_B \times N_B}$ represent matrixes derived from linear parts of operators $\tilde{\mathcal{N}}$ and $\tilde{\mathcal{B}}$. $\mathbf{C}_{\tilde{\mathcal{N}}} \in \mathbf{R}^N$ and $\mathbf{C}_{\tilde{\mathcal{B}}} \in \mathbf{R}^{N_B}$ are constant vectors independent of $\boldsymbol{\mu}$. $g_{\tilde{\mathcal{N}}} : \mathbf{R}^N \times \mathbf{R}^{N_B} \mapsto \mathbf{R}^N$ is a nonlinear function derived from nonlinear part of operator $\tilde{\mathcal{N}}$.

For the treatment of boundary conditions, it can classified into two categories, namely weakly enforced and strongly enforced boundary conditions. As for weakly enforced boundary conditions, no DOFs are required to deploy on the boundaries, i.e. $N_B = 0$, implying a vanishing of $\boldsymbol{\phi}_h^B$ and also Eq. (5). As for strongly enforced boundary conditions, a suitable collocation of DOFs on boundaries is necessary. Note that the commonly used boundary conditions always linear ones, such as Dirictlet, Neumann and Robin conditions, and thus \mathcal{B} are always linear operators. Without loss of generality, we restrict ourselves that the mapping in Eq. (2) will retain the linearity of boundary condition operator $\tilde{\mathcal{B}}$ in computational space. Therefore, discretization of the boundary conditions result in a linear system of equations, i.e., Eq. (5).

In what remains, the Chebyshev pseudospectral method, characterized by its outstanding accuracy, is chosen for discretizing Eqs. (3), which will be detailed in the following subsection.

2.1.1. Chebyshev pseudospectral method

In the Chebyshev pseudospectral method, the d -dimensional variable physical domain will be mapped into a unit regular computational domain $\tilde{\Omega} = [-1, 1]^d$, each dimension discretized by $N_p + 1$ Chebyshev-Gauss-Lobatto points,

$$\xi_i = \cos\left(\frac{\pi i}{N_p}\right), \quad 0 \leq i \leq N_p \quad (6)$$

Spatial derivatives in operators $\tilde{\mathcal{N}}$ and $\tilde{\mathcal{B}}$ are approximated with a matrix-vector multiplication in each dimension. In each dimension, the derivatives are approximated as follows:

$$\left. \frac{\partial^s \phi}{\partial \xi^s} \right|_{\xi_i} = \mathbf{D}^s \phi \quad (7)$$

where $\phi = \{\phi_i\}_{i=0}^{N_p}$, s is the order of derivative and \mathbf{D}^s is the s th-order difference matrix of size $(N_p + 1) \times (N_p + 1)$ with entries defined by

$$D_{i,j}^0 = \delta_{ij} \quad 0 \leq i, j \leq N_p, \quad (8)$$

$$\left\{ \begin{array}{l} D_{i,j}^1 = \frac{B_i}{B_j} \frac{(-1)^{i+j}}{2 \sin\left(\frac{(i+j)\pi}{2N_p}\right) \sin\left(\frac{(j-i)\pi}{2N_p}\right)} \quad 0 \leq i, j \leq N_p, i \neq j \\ D_{i,i}^1 = - \sum_{j=0, j \neq i}^{N_p} D_{i,j}^1 \quad 1 \leq i \leq N_p - 1 \\ D_{0,0}^1 = -D_{N_p, N_p}^1 = -\frac{2N_p^2 + 1}{6} \\ B_i = \begin{cases} 2 & i = 0, N_p \\ 1 & 1 \leq i \leq N_p - 1 \end{cases} \end{array} \right., \quad (9)$$

$$D_{i,j}^s = D_{i,k}^1 D_{k,j}^{s-1} \quad 0 \leq i, j, k \leq N_p. \quad (10)$$

For the following simulations of flow problems, the well known $IP_N - IP_{N-2}$ method is adopted to prevent spurious pressure mode from contaminating the flow fields. In the $IP_N - IP_{N-2}$ method, pressure derivative is approximated without boundary points, and thus pressure is approximated with polynomial of two order lower than all other field variables, such as velocity and temperature. All other variables are discretized with Eqs. (8)-(10) except that the first-order difference matrix \mathbf{D}^1 of pressure is replaced with $\hat{\mathbf{D}}^1$ as follows

$$\left\{ \begin{array}{l} \hat{D}_{i,j}^1 = 0 \quad i = 0, N_p \text{ or } j = 0, N_p \\ \hat{D}_{i,i}^1 = \frac{3\xi_i}{2(1 - \xi_i^2)} \quad 1 \leq i \leq N_p - 1 \\ \hat{D}_{i,j}^1 = \frac{(-1)^{i+j}(1 - \xi_j^2)}{2(1 - \xi_i^2)(\xi_i - \xi_j)} \quad 1 \leq i \neq j \leq N_p - 1 \end{array} \right., \quad (11)$$

For more details of the Chebyshev pseudospectral method, we refer the reader to the reference.

2.2. Reduced-order model

As for solving the problem in Eq. (3), full-order model is always suffering from large computational cost since the required degree of freedom N is always very large. Therefore, we are interested in

replacing the full-order model with a well-posed reduced-order model to represent main dynamic of the system. The full-order model is termed as reducible when Eq. (??) can be well approximated with m -dimensional subspace $\mathcal{V} = \mathbf{R}^{N \times m}$. The subspace is spanned by a suitable set of basis vectors $\{\mathbf{V}_i \in \mathbf{R}^N\}_{i=1}^m$. Note that the size of problem will be largely reduced, only if $m \ll N$. The full-order solution of the interior DOFs ϕ_h can be projected into the subspace \mathcal{V}

$$\phi_h = \mathbf{V}\boldsymbol{\alpha} + \tilde{\phi} + \boldsymbol{\epsilon} \approx \mathbf{V}\boldsymbol{\alpha} + \tilde{\phi} \quad (12)$$

where $\mathbf{V} \in \mathbf{R}^{N \times m}$ is a matrix with the basis vectors as its columns, $\boldsymbol{\alpha}$ is the coefficients of the basis, $\boldsymbol{\epsilon}$ is the projection error, $\mathbf{I} \in \mathbf{R}^N$ is filled with 1. $\tilde{\phi} \in \mathbf{R}$ is independent of $\boldsymbol{\mu}$, set for filtering a constant value to avoid its domination on the basis, and usually it can be set as the average. The boundary conditions say that the interior DOFs have a linear relationship with interior DOFs. Thus, we can enforce the boundary conditions without any reduction. The procedure keeps the reduced-order model of high accuracy at boundaries and avoid shifting of boundary values. According to Eq.(5), the boundary DOFs can be denoted as follows

$$\phi_h^B = -(\mathbf{L}_{\tilde{B}}^B)^{-1} (\mathbf{L}_{\tilde{B}} \phi_h + \mathbf{C}_{\tilde{B}}) \quad (13)$$

Substituting Eq. (12) and (13) into Eq. (4), we have the overdetermined system for interior DOFs

$$\mathbf{L}_{\tilde{N}} \mathbf{V} \boldsymbol{\alpha} + \mathbf{g}_{\tilde{N}} \left(\mathbf{V} \boldsymbol{\alpha} + \tilde{\phi} + \boldsymbol{\epsilon}, -(\mathbf{L}_{\tilde{B}}^B)^{-1} (\mathbf{L}_{\tilde{B}} \mathbf{V} \boldsymbol{\alpha} + \mathbf{C}_{\tilde{B}} + \mathbf{L}_{\tilde{B}} \mathbf{I} \tilde{\phi} + \mathbf{L}_{\tilde{B}} \boldsymbol{\epsilon}) \right) + \mathbf{L}_{\tilde{N}} \mathbf{I} \tilde{\phi} + \mathbf{L}_{\tilde{N}} \boldsymbol{\epsilon} + \mathbf{C}_{\tilde{N}} = 0 \quad (14)$$

For the sake of clarity, Eq. (14) can be rearranged in the simplified form

$$\mathbf{L} \mathbf{V} \boldsymbol{\alpha} + g(\mathbf{V} \boldsymbol{\alpha}) + \mathbf{C} = \tilde{\boldsymbol{\epsilon}} \quad (15)$$

where $\mathbf{L} \in \mathbf{R}^{N \times N}$, $\mathbf{C} \in \mathbf{R}^N$ and $g : \mathbf{R}^N \mapsto \mathbf{R}^N$ is the matrix, vector and function derived from Eq. (14), respectively. The quantity $\tilde{\boldsymbol{\epsilon}}$ represent the residual resulting from the projection error $\boldsymbol{\epsilon}$. In the framework of a Petrov-Galerkin projection, if we consider a basis $\mathbf{W} \in \mathbf{R}^{N \times m}$ that is orthogonal to the residual, the overdetermined system is reduced to a system of m equations

$$\mathbf{W}^T (\mathbf{L} \mathbf{V} \boldsymbol{\alpha} + g(\mathbf{V} \boldsymbol{\alpha}) + \mathbf{C}) = 0 \quad (16)$$

In this work, we restrict ourself to Galerkin framework, namely $\mathbf{W} = \mathbf{V}$. Thus, we have the reduced-order model as follows:

$$\mathbf{V}^T (\mathbf{L} \mathbf{V} \boldsymbol{\alpha} + g(\mathbf{V} \boldsymbol{\alpha}) + \mathbf{C}) = 0 \quad (17)$$

As discussed above, the key point of the reduced-order model is to get a suitable basis. In the literature, there exists many methods to achieve it. Such popular methods includes, but not limited to, the Proper Orthogonal Decomposition (POD), the Proper Generalized Decomposition, the Piecewise Tangential Interpolation, the Matrix Interpolation, the Loewner framework and several greedy-based approaches for the identification of sub-optimal subspaces. Among these methods, POD, perhaps the most widely used technique, is described and employed in the following.

2.2.1. POD reduced basis

The Proper Orthogonal Decomposition (POD) is one of the most widely used techniques to compress data and extract fundamental information by building a series of orthogonal basis with decreasing energy distribution. Let $\mathcal{P}_M = \{\boldsymbol{\mu}_1, \boldsymbol{\mu}_2, \dots, \boldsymbol{\mu}_M\} \subset \mathcal{P}$ be a discrete and finite set of M parameters generated with a suitable sampling method, and $\Phi_{\mathcal{P}_M} = \{\phi_h(\boldsymbol{\mu}_1), \phi_h(\boldsymbol{\mu}_2), \dots, \phi_h(\boldsymbol{\mu}_M)\} \in \mathbf{R}^{N \times M}$ be the corresponding snapshot matrix obtained by full-order method. Consider that snapshot

matrix $\Phi_{\mathcal{P}_M}$ can represent the underlying physics dynamics of the problem. The idea behind POD technique is to find a suitable orthogonal basis matrix to minimise the problem defined as follows:

$$\begin{aligned} \min_{\mathbf{V} \in \mathbf{R}^{N \times m}} \quad & \|\Phi_{\mathcal{P}_M} - \mathbf{V}\mathbf{V}^T\Phi_{\mathcal{P}_M}\|_F, \\ \text{s.t.} \quad & \mathbf{V}^T\mathbf{V} = \mathbf{E}, \end{aligned} \quad (18)$$

where \mathbf{E} is the identify matrix of size M and $\|\cdot\|_F$ is the Frobenius norm. Galerkin is a popular choice of projection. According to the Eckart-Young theorem, the solution of Eq. (18) is exactly the first m th left singular vectors of the matrix $\Phi_{\mathcal{P}_M}$, derived from singular value decomposition which reads

$$\Phi_{\mathcal{P}_M} = \mathbf{U}_S \Sigma_S \mathbf{V}_S, \quad \Sigma_S = \text{diag}(\sigma_i) \quad (19)$$

where the singular values σ_i , $1 \leq i \leq \min(N, M)$ are sorted in a decreasing order. Choosing the first m th columns of \mathbf{U}_S , we have an error estimation of Eq. (18) as

$$\min_{\mathbf{V} \in \mathbf{R}^{N \times m}} \|\mathbf{S} - \mathbf{V}\mathbf{V}^T\mathbf{S}\|_F^2 = \sum_{i=m+1}^{\min(N, M)} \sigma_i^2 \quad (20)$$

In Eq. (20), it is shown that the error is exactly made up with the squares of the neglected singular values. That is to say, with a suitable m , we can approximate the snapshot matrix $\Phi_{\mathcal{P}_M}$ at an arbitrary accuracy. Luckily, most problems exhibit an exponentially decaying series of singular values, and thus we can chose a very small value of m to approximate the problems with a good accuracy.

2.2.2. Further reduction in online cost

Although we have the reduced-order model defined in Eq. (17), the computational cost is still very expensive, scaling with the original size of teh full-order model. For online stage, a further reduction of computational cost is required. For linear parts in Eq. (17), they can be treated as follows

$$\begin{aligned} \mathbf{V}^T \mathbf{L} \mathbf{V} \boldsymbol{\alpha} &= \tilde{\mathbf{L}} \boldsymbol{\alpha} \\ \mathbf{V}^T \mathbf{C} &= \tilde{\mathbf{C}} \end{aligned} \quad (21)$$

where $\tilde{\mathbf{L}} \in \mathbf{R}^{m \times m}$ and $\tilde{\mathbf{C}} \in \mathbf{R}^m$ can only be computed once with the knowledge of basis matrix \mathbf{V} . Therefore, the online calculation of linear parts scales with m . However, the drawback of the reduced-order model is that the cost of exact evaluation of nonlinear part $\mathbf{V}^T g(\mathbf{V}\boldsymbol{\alpha})$ in Eq. (17) scales with N , namely the size of full-order model. To tackle this defect, several hyper-reduction methods have been developed in the last decades to enable significant speedups for nonlinear part. These methods tries to find the optimal tradeoff between accuracy and efficiency. Such methods include but not limited to the Empirical Interpolation method (EIM), its discrete variant (DEIM), Gappy-POD and Missing Point Estimation (MPE). In the present work, we restrict ourselves to quadratic nonlinearity, which can be exactly transformed to quadratic form, and thus hyper-reduction is avoid. Consider a common quadratic nonlinearity

$$g(\mathbf{V}\boldsymbol{\alpha}) = (\mathbf{V}\boldsymbol{\alpha}) \otimes (\mathbf{V}\boldsymbol{\alpha}) \quad (22)$$

where \otimes denotes element-wise multiplication operator. Substituting Eq. (22) in to Eq. (17), the nonlinear part can be transformed as

$$\mathbf{V}^T g(\mathbf{V}\boldsymbol{\alpha}) = \mathbf{V}^T ((\mathbf{V}\boldsymbol{\alpha}) \otimes (\mathbf{V}\boldsymbol{\alpha})) = \sum_{k=0}^m (\boldsymbol{\alpha}^T \mathbf{A}^k \boldsymbol{\alpha}) \mathbf{E}_k, \quad 0 \leq k \leq m \quad (23)$$

where $\mathbf{E}_k \in \mathbf{R}^m$ is k th column of the unit matrix \mathbf{E} , $\mathbf{A}^k \in \mathbf{R}^{m \times m}$ is calculated as

$$\mathbf{A}_{i,j}^k = \mathbf{V}_k \cdot (\mathbf{V}_i \otimes \mathbf{V}_j), \quad 0 \leq i, j, k \leq m \quad (24)$$

where \mathbf{V}_i , \mathbf{V}_j and \mathbf{V}_k are the i th, j th and k th columns of \mathbf{V} , respectively.

3. Physics-informed machine learning of reduced-order model

This section presents several methods aiming to find the mapping from parameter space to high-fidelity solution. Based on the reduced basis, we just need to find the mapping from parameter space to reduced basis coefficient, namely the projection of high-fidelity solution onto reduced basis. These methods are classified into intrusive and non-intrusive methods. We term it as a non-intrusive method if the reduced-order model won't need to be built, otherwise it is an intrusive method. As for non-intrusive methods in reference ??, the underlying idea is an interpolation, such as the projection-driven neural network(PDNN) proposed by Jan ?? and the traditional cubic spline method. These non-intrusive methods can achieve a good approximation with very little online cost, but the drawback is their highly relying on the size of labeled data set, namely the number of evaluations of full-order model. For example, the traditional cubic spline method requires high-fidelity solutions with a tensor-product grid in parameter space, and the POD-NN are trained with a labeled data set. According to Jan, the PDNN has a good reduction in the eagerness of more labeled data compared with the cubic spline method. Even so, the required size of labeled data for the PDNN is prohibitively larger than the size of snapshots for building a satisfactory reduced basis.

A good alternate is the intrusive method, feathering a much cheaper computational cost of the reduced-order model. One can directly solve the reduced-order model with a suitable nonlinear solver, such as Newton-like method. However, it is also a tough work to find the right solution especially for a larger number of reduced-order model, as a reasonable initial solution is not always available. To this end, we combine artificial network (ANN) and the reduced-order model together together, benefiting from the cheap cost of reduced-order mode and powerful approximating capability of ANN. We first propose to solve the reduced-order model with ANN, referred to physics-informed network (PINN). Then we try to add more prior knowledge into reinforce the PINN, referred to physics-reinforced neural network (PDNN). For the sake of clarity, the relationships of these methods are illustrated in Fig. 1.

In the next subsections, we first briefly introduce the basic idea of artificial neural networks. Then we will start from the projection-driven neural networks proposed by Jan ??. After that, the proposed physics-inform neural network and physics-reinforced neural network will be detailed.

3.1. Artificial neural network (ANN)

For an arbitrary target function, ANN is a powerful nonlinear approximator constituted of a linear combination of some nonlinear functions. Generally, ANN contains L hidden layers besides input and output layers, the i th layer equipped with n_i neurons, where $l = 0, 1, \dots, L+1$ denotes the input layer, 1st hidden layer, ..., L th hidden layer and the output layer, respectively. ANN is a nonlinear function $\mathcal{O} : \mathbf{R}^{n_0} \mapsto \mathbf{R}^{n_{L+1}}$ of inputs \mathbf{x} , comprising a recursion

$$\begin{cases} \mathcal{O}^0 = \mathbf{x} \\ \mathcal{O}^l = \sigma^l (\mathbf{W}^l \mathcal{O}^{l-1} + \mathbf{b}^l) \end{cases} \quad 1 \leq l \leq L+1 \quad (25)$$

where $\mathcal{O}^l \in \mathbf{R}^{n_l}$ is the output of l th layer, n_0 is the input dimension and n_{L+1} is the output dimension, $\mathbf{W}^l \in \mathbf{R}^{n_l \times n_{l-1}}$ is the weights, $\mathbf{b}^l \in \mathbf{R}^{n_l}$ is the biases and σ^l is an element-wise activation function. Usually, the activation function of the output layer is just set as the identification function, namely $\sigma^{L+1}(\mathbf{x}) = \mathbf{x}$, while the activation function of all hidden layers are set as a same nonlinear function.

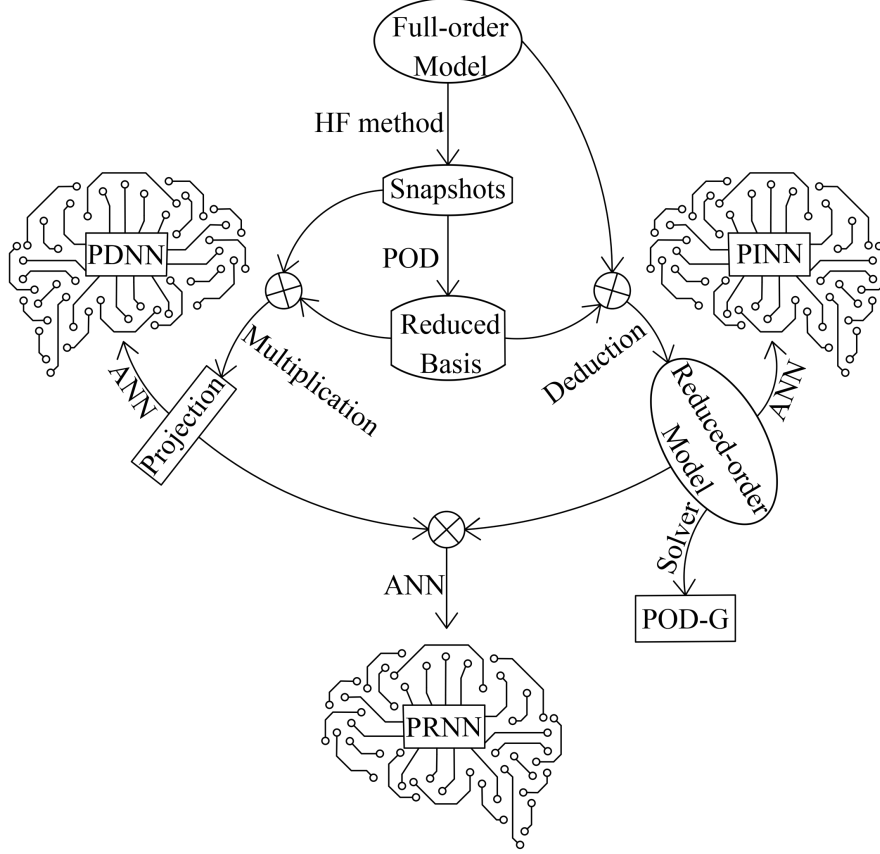


Figure 1: Relationship among methods

In this work, we simply set the activation function as Swish function $\text{Swish}(x) = x\text{sigmoid}(x)$ and use the same number of neurons in each hidden layers $n_1 = n_2 = \dots = n_L = n_H$, if not stated otherwise. For a specific ANN architecture (L the network depth and n_H the network width), the weights and biases of ANN are trained to minimize the discrepancy between ANN outputs and targets for the given inputs, where the discrepancy is metricate by a scalar loss function. Thus the training of ANN is essentially an single-objective minimization problem

$$\arg \min_{\mathbf{W}, \mathbf{b}} \text{loss}(\mathcal{O}(\mathbf{x}), \mathcal{O}_{\text{target}}(\mathbf{x})). \quad (26)$$

However, optimizing the minimization problem is not trivial. As for approximating a complex nonlinear target function with high dimensional inputs/outputs, an ANN of large depth and width is always necessary, resulting in a much larger size of independent variables in \mathbf{W}, \mathbf{b} , where $\mathbf{W} = \{\mathbf{W}_i\}_{i=1}^{L+1}$ and $\mathbf{b} = \{\mathbf{b}_i\}_{i=1}^{L+1}$. Thus many numerical issues will emerge, among which local minima and overfitting traps are the most common cases. Luckily, many training techniques have been developed in last decades, such as Mini-Batch method to relive local minima trap and regulation method to relieve overfitting trap.

3.2. Customized networks

Some preparation need to be made before introducing the networks. Recall that the snapshot set $\Phi_{\mathcal{P}_M} = \{\phi_h(\mu_1), \phi_h(\mu_2), \dots, \phi_h(\mu_M)\} \in \mathbf{R}^{N \times M}$ corresponding with the parameter set $\mathcal{P}_M =$

$\{\boldsymbol{\mu}_1, \boldsymbol{\mu}_2, \dots, \boldsymbol{\mu}_M\} \subset \mathcal{P}$ is employed to extract the reduced basis \mathbf{V} , according to Section 2.2. Due to the orthogonality of \mathbf{V} , the projection coefficient of each snapshot on the reduced space is derived by left multiplying Eq. (12) with \mathbf{V}^T

$$\begin{aligned}\boldsymbol{\alpha} &= \mathbf{V}^T(\boldsymbol{\phi}_h - \tilde{\boldsymbol{\phi}} - \boldsymbol{\epsilon}) \\ &\approx \mathbf{V}^T(\boldsymbol{\phi}_h - \tilde{\boldsymbol{\phi}})\end{aligned}\quad (27)$$

All the parameters in \mathcal{P}_M along with the projections of their corresponding snapshots, denoted by $\mathcal{D}_{Pr} = \left\{ \left(\boldsymbol{\mu}_i, \boldsymbol{\alpha}|_{\boldsymbol{\mu}=\boldsymbol{\mu}_i} \right) \right\}_{i=1}^M$, will be a good collection of input-output data set for training an ANN. As the projection is the best approximation to the snapshot with only the projection error, the data set \mathcal{D}_{Pr} is the best choice for training an ANN.

As ANN is sensitive to the difference in dimensional scale of inputs/outputs, the data set \mathcal{D}_{Pr} need to be further normalized before feeding it into the ANN. For inputs, namely $\boldsymbol{\mu} \in \mathcal{P}$, as the range of the parameter space is always acknowledged, the minimal and maximal of the parameter space can be utilized to scale the inputs to $[-1, 1]^{n_0}$, which is formulated as follows

$$\tilde{\boldsymbol{\mu}}(\boldsymbol{\mu}) = \frac{\boldsymbol{\mu} - (\boldsymbol{\mu}_{\max} + \boldsymbol{\mu}_{\min})/2}{(\boldsymbol{\mu}_{\max} - \boldsymbol{\mu}_{\min})/2} \quad (28)$$

We note that the division in Eq. (28) denotes an element-wise operation, and it also applies in the following. As for the outputs, there is not an prior range of the output, however. We turn to a statistical method do the normalization with an assumption that the outputs satisfy the Gaussian distribution. To this end, the standard derivation $\boldsymbol{\Theta}$ and mean $\bar{\boldsymbol{\alpha}}$ are calculated, and then the outputs are normalized as follows

$$\tilde{\boldsymbol{\alpha}}(\boldsymbol{\alpha}) = \frac{\boldsymbol{\alpha} - \bar{\boldsymbol{\alpha}}}{\boldsymbol{\Theta}} \quad (29)$$

We wrap the normalisation of inputs/outputs into the ANN as follows

$$\tilde{\mathcal{O}}(\boldsymbol{\mu}; \mathbf{W}, \mathbf{b}) = \mathcal{O}(\tilde{\boldsymbol{\mu}}(\boldsymbol{\mu})) \otimes \boldsymbol{\Theta} + \bar{\boldsymbol{\alpha}} \quad (30)$$

Thus, the inputs and outputs of the wrapped network $\tilde{\mathcal{O}}(\bullet)$ will be physical variables, while the inputs and outputs of the original network $\mathcal{O}(\bullet)$ will be normalized variables.

3.2.1. Projection-driven neural network(PDNN)

According to Jan ??, the data set \mathcal{D}_{Pr} is used directly to train the network to avoid building the reduced-order model. The data set \mathcal{D}_{Pr} is randomly split into two parts: train set \mathcal{D}_{Pr}^{tr} and validation set \mathcal{D}_{Pr}^{te} . The famous Adam optimizer is employed to train the network. The ratio between the size of \mathcal{D}_{Pr}^{tr} and \mathcal{D}_{Pr} is set as 0.7. The loss function is defined as the mean square error between network outputs and targets scaled with the standard derivation $\boldsymbol{\Theta}$, namely

$$loss_{PDNN} = \frac{1}{N_{\mathcal{D}}} \sum_{\boldsymbol{\mu}, \boldsymbol{\alpha} \in \mathcal{D}} \left\| \frac{(\tilde{\mathcal{O}}(\boldsymbol{\mu}; \mathbf{W}, \mathbf{b}) - \boldsymbol{\alpha})}{\boldsymbol{\Theta}} \right\|^2 \quad (31)$$

where \mathcal{D} is the chosen data set of size $N_{\mathcal{D}}$, which can be the train set or the test set.

In real applications, we are not expected to generate too many snapshots, since the full-order model is always prohibitively expensive. Thus the data set size \mathcal{D}_{Pr} is always to very small, so the training of the network will get trapped into overfitting problem. To prevent overfitting, first the L_2 regulation technique is employed by penalizing the loss of the train set with the weights \mathbf{W}

$$\widetilde{loss}_{PDNN} = loss_{PDNN} + \eta \|\mathbf{W}\|^2 \quad (32)$$

where η is the decay weight. Besides, we adopt the early stopping criterion: training will be immediately stopped only if the validation loss keeps increasing over K_{early} epoches. In what remains, $\eta = 10^{-4}$ and $K_{early} = 6$ are employed.

3.2.2. Physics-informed neural network(PINN)

Due to the limited number of available snapshots, it is always difficult to train a good network with Projection-driven neural network. Luckily, we have the reduced-order model, an another choice for training an ANN. Given the reduced-order model, ANN outputs don't explicitly approximate some given targets, but just do satisfy the reduced-order model. In this way, no target is needed, and thus we have unlimited training data. By Latin hypercube sampling in parameter space, we generate the data set $\mathcal{D}_{Resi} = \{\boldsymbol{\mu}_i\}_{i=1}^{M_{Resi}}$, constraining M_{Resi} residual points in parameter space. The loss function is defined as follows

$$loss_{PINN} = \frac{1}{N_{\mathcal{D}}} \sum_{\boldsymbol{\mu} \in \mathcal{D}} \left\| ROM \left(\tilde{\mathcal{O}}(\boldsymbol{\mu}; \mathbf{W}, \mathbf{b}) \right) \right\|^2 \quad (33)$$

where $ROM(\boldsymbol{\alpha}) = \mathbf{V}^T (\mathbf{L}\mathbf{V}\boldsymbol{\alpha} + g(\mathbf{V}\boldsymbol{\alpha}) + \mathbf{C})$ is the reduced-order model defined in Eq. (17). As we have unlimited training data, there is no problem of overfitting and thus no need of validation data set. The bottleneck of training the physics-informed neural network is how to handle the local minima trap. Here, we adopt the Mini-Batch training method, where the data set are shuffled and randomly in to serval non-overlap subsets in each epoch. With each subset, the weights and biases will be updated by optimizer. The Mini-Batch training method can effectively avoid local minima trap and has enjoyed a great number of applications.

3.2.3. Physics-reinforced neural network(PRNN)

Physics-informed neural network(PINN) seems an perfect potential in prediction reduced basis coefficients. But the numerical experiments show that the accuracy of the physics-informed neural network sometimes is not that good, even if the the corresponding loss drops down to a very low level. The underlying reason comes from that the large scale difference of different RB modes. First, the RB mode with smaller index will be more dominant to the residual of the reduced-order model. Second, the training of network cannot work like a deterministic nonlinear solver, and it can only reduce the loss to a moderate level. Thus, the reduced-order model cannot be well-solved thorough training network. As a result, the optimizer tends to neglect the relatively unimportant modes, namely the high-index modes.

To address this problem, we add the projection RB coefficients into the loss function of PINN. Although the projection RB coefficients are always not the solutions of the reduced-order model, the projections are more close to the snapshots and thus full-order model. Besides, the projection RB coefficients can be calculated directly according to Eq. 27, and it has no problem of domination for different modes. Therefore, the projection RB coefficients can be used to provide more physical information into the network training. Thus we name this method as physics-reinforced neural network. The loss function is defined as the weighted sum of those of PDNN and PINN, namely

$$loss_{PRNN} = loss_{PDNN}|_{\mathcal{D}=\mathcal{D}_{Pr}} + w \times loss_{PINN}|_{\mathcal{D}=\mathcal{D}_{Resi}} \quad (34)$$

where w is a specific weight balancing projection and reduced-order model. In this work, we find that simply setting $w = 1$ will produces a good result. When training the network, the two data sets are treated separately. As for projection data set \mathcal{D}_{Pr} , it is more accurate but its size is very small, so we continue to use full batch. As for residual data set \mathcal{D}_{Pr} , it is less accurate but its size is very large, and we use mini-batch method for each updating of the network.

4. Numerical results

In this section, we will discuss the application of PDNN, PINN and PRNN methods to the parameterized PDEs, namely the one-dimensional Burges' equation, two-dimensional lid driven flow and two-dimensional natural convection flow. The one-dimensional case are designed with an

artificial solution with a zero-value boundary condition, intended for testing the prediction accuracy of the three networks and also study the influence of several factors. Their prediction accuracy are further discussed the two realistic flow problems, where geometry parameters and common boundary conditions (Dirichlet and Neumann) are included.

For comparison of accuracy, the results of two analytical methods are also considered:

- (1) **Projection**: Projection of high-fidelity solution onto reduced basis;
- (2) **POD-G**: The solution of the reduced-order model.

As the PDNN is trained with the projection coefficients of high-fidelity, the PDNN targets the accuracy of the Projection. The PINN is trained to meet the reduced-order model, the PINN targets the accuracy the POD-G. The PRNN can be viewed as a blending of the PDNN and PINN, and thus its accuracy is expected to fall somewhere between those of the Projection and POD-G.

To assess the online accuracy of these methods, the following metrics are defined in the sense of mean squared error.

- (1) the average relative error of projections

$$\varepsilon_{\text{Proj}} = \frac{1}{N_{\mathcal{D}_{te}}} \sum_{\boldsymbol{\mu}, \boldsymbol{\phi}_h \in \mathcal{D}_{te}} \frac{\|\boldsymbol{\phi}_h - \tilde{\boldsymbol{\phi}} - \mathbf{V}\mathbf{V}^T(\boldsymbol{\phi}_h - \tilde{\boldsymbol{\phi}})\|}{\|\boldsymbol{\phi}_h - \tilde{\boldsymbol{\phi}}\|} \quad (35)$$

- (2) the average relative error of POD-G solutions

$$\varepsilon_{\bullet} = \frac{1}{N_{\mathcal{D}_{te}}} \sum_{\boldsymbol{\mu}, \boldsymbol{\phi}_h \in \mathcal{D}_{te}} \frac{\|\boldsymbol{\phi}_h - \tilde{\boldsymbol{\phi}} - \mathbf{V}\boldsymbol{\alpha}_{\bullet}(\boldsymbol{\mu})\|}{\|\boldsymbol{\phi}_h - \tilde{\boldsymbol{\phi}}\|} \quad (36)$$

where $\mathcal{D}_{te} = \{\boldsymbol{\mu}_i, \boldsymbol{\phi}_h(\boldsymbol{\mu}_i)\}_{i=1}^{N_{\mathcal{D}_{te}}}$ is the test data set of size \mathcal{D}_{te} , the subscript " \bullet " is used to take the place of "POD-G", "PDNN", "PINN" and "PRNN". Thus, $\boldsymbol{\alpha}_{\bullet}(\boldsymbol{\mu})$ is the solution calculated from the corresponding method.

Note that the Projection, POD-G, PDNN, PINN and PRNN methods are all coded in Python. The networks built are all under the framework of Pytorch. The training of networks are all implemented on two GUPs (NVIDIA Quadro GP100) of a server class station. To solve the reduced-order model directly for POD-G, the nonlinear solver "linalg.solve" in Numpy library is employed. We refer the reader to the repository ¹ for further details of the code method. For different data set as discussed above, we employ the specific sampling methods in parameter space: for building the RB, we adopt the Sobol sequences, a quasi-random low-discrepancy sequences; For choosing residual points, we use the Latin hypercube sampling; For generating test data set, we employ uniformly tensor-product grid.

4.1. Burgers' equation

In this subsection, to validate the proposed methods, we consider the one-dimensional parameterized Burgers' equation.

$$\begin{cases} \phi(x; \boldsymbol{\mu}) \cdot \nabla \phi(x; \boldsymbol{\mu}) - \Delta \phi(x; \boldsymbol{\mu}) = s(x; \boldsymbol{\mu}) & -1 \leq x \leq 1 \\ \phi(x = \pm 1; \boldsymbol{\mu}) = 0 \end{cases} \quad (37)$$

¹available at <https://github.com/cwq2016/POD-PINN>

where $\boldsymbol{\mu} = (\mu_1, \mu_2) \in [1, 10] \times [1, 10]$ and $s(x; \boldsymbol{\mu})$ is the source term defined so that the exact solution satisfies

$$\phi(x; \boldsymbol{\mu}) = (1 + \mu_1 x) \sin(-\mu_2 x/3)(x^2 - 1). \quad (38)$$

For each parameter, the solution at the two end points are simply set zero to avoid the influence of boundary conditions. The problem is solved with Chebyshev pseudospectral(PS) method with $N_p + 1 = 128 + 1$ Chebyshev Gauss-Lobatto points.

We are interested in the prediction accuracy of the Projection, POD-G, PDNN, PINN and PRNN methods. The accuracy of Projection and POD-G is only determined by two factors, namely the sample size N_s for building RB and the number of chosen modes m , provided that the nonlinear solver for POD-G is accurate enough. Here we term the two factors as essential factors. Besides the two factors, neural network like PDNN, PINN and PRNN are also determined by network architecture, the number of residual points, and so on. To study the influence of these factors, we resort to the control variates method. Some base values are set for these factor, namely sample size is $N_s = 80$, the number of chosen modes is picked from the set $\{2, 3, \dots, 9\}$, network architecture is $L = 3$ and $n_H = 20$, the number of residual points is $N_{Resi} = 5000$. To test the prediction accuracy, a test data set of size $101 \times 101 = 10201$ is generated on a tensor-product parameter grid $\{1 + 0.09i\}_{i=0}^{100} \times \{1 + 0.09i\}_{i=0}^{100}$. The dense test grid will guarantee the reliability of the prediction accuracy. As for the training of networks, we use the same following hyperparameters: 20000 epoches, 10 batches with each batch of size $N_{Resi}/10$, the leaning rate initialized as 0.01 and decaying by 96% every 200 epoches.

We first study the influence of the sample size. Fig. 2, presents the singular value distribution for the sample number $N_s = 80$. It is shown that the singular value decays quickly, implying that a small number of RB modes is enough for representing the dynamic of the problem. Meanwhile, the sample number can also be largely reduced. Thus, for comparison, $N_s = 10$ and 320 random parameter samples are independently generated with Sobol sequences. The five methods are applied to the problem after the RB are built for $N_s = 10, 80$ and 320, respectively. The prediction accuracy is shown in Fig. 3. It is shown that the Projection enjoys a better accuracy compared with the POD-G, but their discrepancy is very small. The pojection/POD-G improves just a little for sample number N_s increasing from 10 to 80, and almost stagnates from $N_s = 80$ to 320. Thus, sample number $N_s = 10$ is enough for capture the main dynamic of the problem. The networks perform quite differently. The accuracy of PDNN is far lower than that of PINN and PRNN. Even with the increase of sample number, the accuracy of PDNN can improve by one order of magnitude, but the error curves fluctuate intensively especially for larger m . On the contrary, both PINN and PRNN perform much better, they almost keep pace with POD-G for smaller m . As $m \geq 6$, the PINN performs a little better than the PRNN, but their error level both come to a saturation and cannot further drop down. The reason for the saturation is that both the PINN and PRNN can only reduce their loss function down to a level of 10^{-6} for this problem rather than zero or machine zero level. Thus the high-index modes of little importance are neglected by the networks. The PINN performs a little better than the PRNN, which is opponent with our inference in Section 3.2.3. The reason is two-fold: first, the problem and the target function is relatively easy for networks; second, the accuracy of POD-G is very close to projection. Therefore, There is no priority for the PRNN, as its loss function is a hybrid.

To further study the influence of network architecture on the prediction accuracy of the three networks, we change network width to $n_H = 10$ and $n_H = 30$, respectively, while keeping network depth $L = 3$ fixed. The results are shown in Fig. 4. It is shown that the PDNN can not gain an improvement of accuracy with the increase of n_H , or even get rid of the fluctuation, resulting from the overfitting trap. On the contrary, the PINN and PRNN show a much better tendency. Their prediction accuracy increases with n_H but tends to saturate for a larger n_H . This is in accordance with the situation that the approximation capability of the network increases and gradually saturate with network size.

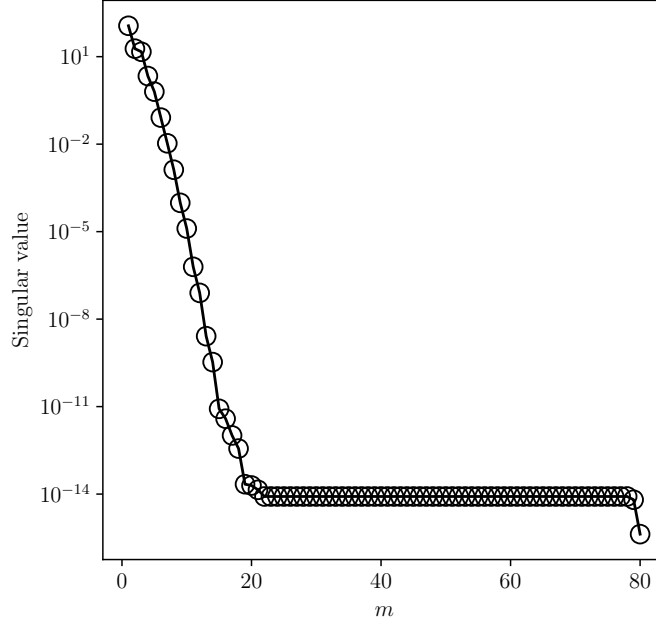


Figure 2: Singular value distribution of 80 snapshots for 1D Burges' equation

As there are unlimited residual points available for training both the PINN and PRNN, we are interested in how the number of residual points influence the prediction accuracy. In addition to $N_{Resi} = 5000$, the numbers of residual points $N_{Resi} = 1250, 2500$ and 10000 are considered, and the results are shown in Fig. 5. The influence of the number of residual points is similar with that of network architecture. That is to say, the prediction accuracy increases with the number of residual points N_{Resi} , but it will reach a saturation after some critical N_{Resi} .

Besides, the further confirmation of the reliability of PRNN is shown in Fig. 6, offering a good agreement between the Chebyshev pseudospectral method and PRNN for some specific parameters.

4.2. Lid-driven cavity

The lid-driven cavity flow is considered for testing the prediction accuracy of the proposed methods in handling realistic problem. The flow is governed by the following non-dimensional incompressible Navier-Stokes equations

$$\begin{cases} \nabla_{\mathbf{x}} \cdot \mathbf{u} = 0 \\ (\mathbf{u} \cdot \nabla_{\mathbf{x}}) \mathbf{u} = -\nabla_{\mathbf{x}} p + \frac{1}{Re} \nabla_{\mathbf{x}}^2 \mathbf{u} \end{cases}, \quad (39)$$

where $\mathbf{u} = (u, v)$ is the dimensionless velocity in Cartesian coordinate $\mathbf{x} = (x, y)$, p is the pressure, ∇ is the Hamiltonian operator, Re is the Reynolds number. The geometry of the problem is depicted in Fig. 7(a), which is affected by the inclining angle θ of the left and right side walls. The Reynolds number and the inclining angle are the parameter $\boldsymbol{\mu}$ controlling the problem. In order to address the variable geometry, the physical domain is mapped to an square domain $[-1, 1]^2$. The mapping \mathcal{X} from the physical domain $\mathbf{x} \in \Omega(\boldsymbol{\mu})$ to the computation domain $\boldsymbol{\xi} = (\xi_1, \xi_2) \in [-1, 1]^2$ and its inverse \mathcal{X}^{-1} are defined as follows:

$$\mathcal{X} : \begin{cases} x = 1/2\xi_1 + 1/2\xi_2 \cos(\theta) \\ y = 1/2\xi_2 \sin(\theta) \end{cases} \quad \Rightarrow \quad \mathcal{X}^{-1} : \begin{cases} \xi_1 = 2(x - y \cot(\theta)) \\ \xi_2 = 2y/\sin(\theta) \end{cases} \quad (40)$$

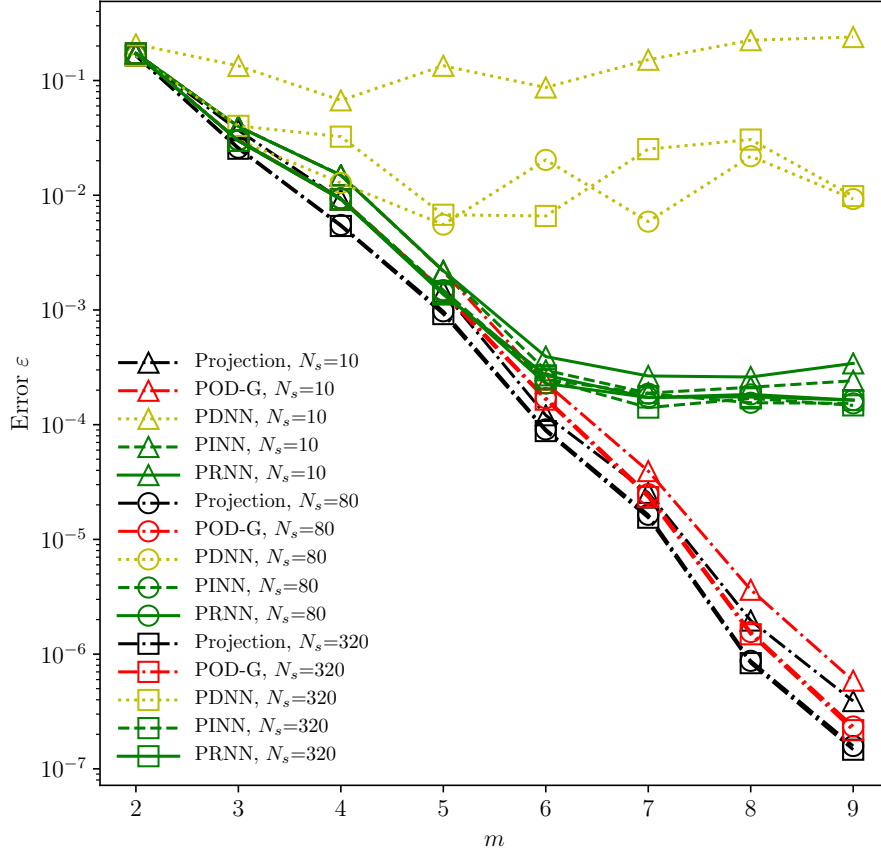


Figure 3: The prediction accuracy of the Projection, POD-G, PDNN, PINN and PRNN methods for the number of snapshots $N_s=10, 80$ and 320 , respectively.

Thus, we have the Jacobin matrix of the mapping

$$\mathbf{J} = \frac{\partial \mathbf{x}}{\partial \boldsymbol{\xi}} = \begin{bmatrix} 2 & 0 \\ -2 \cot(\theta) & 2/\sin(\theta) \end{bmatrix} \quad (41)$$

Substituting Eq. 41 into Eq. 39, we have the governing equation in computational space:

$$\begin{cases} (\mathbf{J}^{-1} \nabla_{\boldsymbol{\xi}}) \cdot \mathbf{u} = 0 \\ (\mathbf{u} \cdot (\mathbf{J}^{-1} \nabla_{\boldsymbol{\xi}})) \mathbf{u} = -(\mathbf{J}^{-1} \nabla_{\boldsymbol{\xi}}) p + \frac{1}{Re} (\mathbf{J}^{-1} \nabla_{\boldsymbol{\xi}})^2 \mathbf{u} \end{cases} \quad (42)$$

The flow is driven by the top moving wall. All the other three sides are all no-slip walls. The flow is discretized by the Chebyshev pseudospectral method with a tensor-product grid of 49×49 . For this problem, it is crucial to address the well-known difficulty the corner singularity, resulting from the discontinuous horizontal velocity at the two top corners. In this work, to remove the singularity, the velocity of top wall is specified as

$$u_W = (1 + \xi_1)^2 (1 - \xi_1)^2 \quad (43)$$

as adopted in references ???. The $IP_N - IP_{N-2}$ scheme is employed to remove the spurious modes of pressure. Besides, the artificial compressibility method is employed to address the coupling

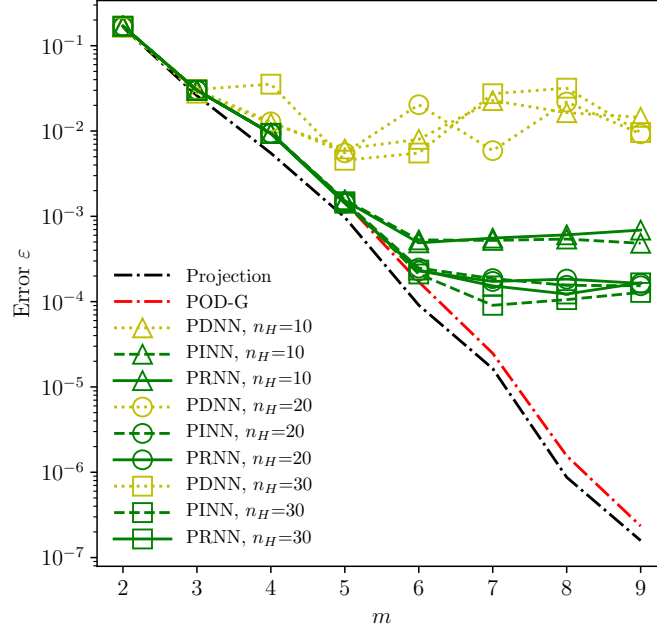


Figure 4: The prediction accuracy of the Projection, POD-G, PDNN, PINN and PRNN methods. The network width is set $n_H = 10, 20$ and 30 , respectively.

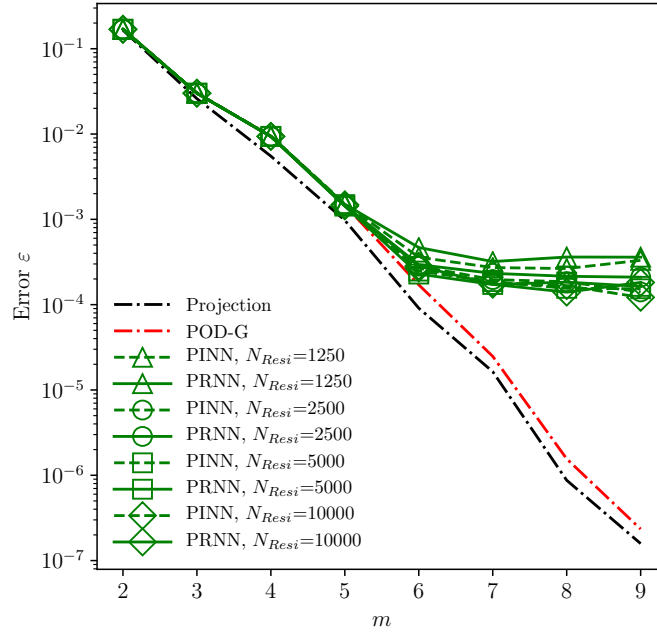


Figure 5: The prediction accuracy of the Projection, POD-G, PINN and PRNN methods. $N_{Resi}=1250, 2500, 5000, 10000$ residual points are chosen for training the PINN and PRNN.

velocity field and pressure by transforming steady Eq. (42) into an unsteady one in pseudo time .

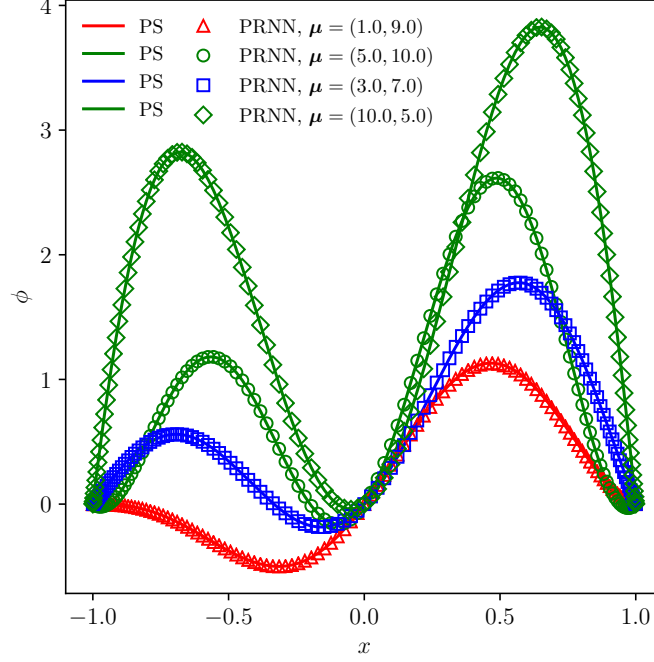


Figure 6: The comparison between the Chebyshev pseudospectral (PS) and the PRNN solutions for four specific parameters. The results of the PRNN are obtained via employing the $m=9$ modes extracted from 10 snapshot and a network of $L=3$ and $n_H=20$ architecture trained with 5000 residual points.

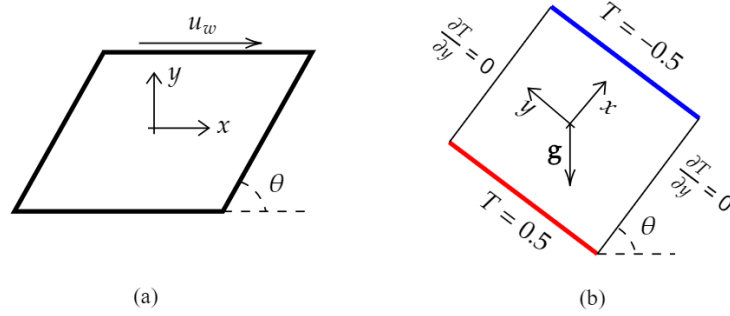


Figure 7: The geometry and boundary conditions for (a) Lid-Driven flow and (b) Natural convection in enclosure.

The derived discrete equation is then solved using an explicit fourth-order four-stage Runge-Kutta integrator in pseudo time.

The parameter space of interest is $\mu = (Re, \theta) \in [100, 500] \times [\pi/3, 2\pi/3]$. 100 snapshots of high-fidelity solutions for parameters generated with Sobol sequence are calculated and collected for building the reduced basis, and the corresponding singular value distribution is plotted in Fig. 8. It is shown that the singular value decays slowly, implying that more modes are required to represent the underlying dynamic. We choose the first $m = 5, 10, \dots, 30$ modes to test the prediction accuracy of PDNN, PINN and PRNN. The prediction accuracy is assessed on a test data set of size $11 \times 11 = 121$, generated on a tensor-product parameter grid $\mu = \{100 + 40i\}_{i=0}^{10} \times \{\pi/3 + j\pi/15\}_{j=0}^{10}$.

For the POD-G method solving the reduced-order model, the solving always blows up if it starts from an improper initialization. In this work, for testing the prediction accuracy of the POD-G method, the solving of the reduced-order model for a parameter μ starts from the projection coefficients of the full-order solution $\phi_h(\mu)$ on the reduced basis. Besides, for the sake of comparison, we pick the first 30, 60 snapshots from the 100 snapshots to do the same test. As for the training of networks, we use the same following hyperparameters: 40000 epoches, batch size 1000, the learning rate initialized as 0.01 and decaying by 96% every 200 epoches.

The prediction accuracy is shown in Fig. 9. It is shown that the POD-G is far from Projection, compared with Fig. 3 for the Burgers' equation. Similar convergence tendency features the PINN and PRNN, i.e. the accuracy increase with smaller m but saturates after a critical value of m . However, the priority of the PRNN over PINN is demonstrated. The PINN will saturate for $m \geq 15$, even if more snapshots are employed for building the reduced basis. On one way, the PINN can achieve an accuracy between the POD-G and Projection for smaller m , conforming the blending construction of the loss function in Eq. (34) of the PRNN; on the other way, the PRNN performs better than PINN, and shows an increase of accuracy with m . The PDNN enjoys an agreement with the Projection for a smaller m , and also an improvement with the increase of m . However, it quickly deteriorates after a critical value of m .

All in all, it can be concluded that the PRNN is much better than the PINN and PDNN. The further confirmation of the reliability of PRNN is shown in Fig. 10, offering a good agreement between the Chebyshev pseudospectral method and PRNN for some specific parameters. We note that the streamlines displayed in Fig. 10 are derived by solving the following Poisson equation for streamfunction with the acknowledged velocity field:

$$\begin{cases} \nabla_{\mathbf{x}}^2 \psi = \frac{\partial u}{\partial y} - \frac{\partial v}{\partial x} & x \in \Omega \\ \psi = 0 & x \in \partial\Omega \end{cases} \quad (44)$$

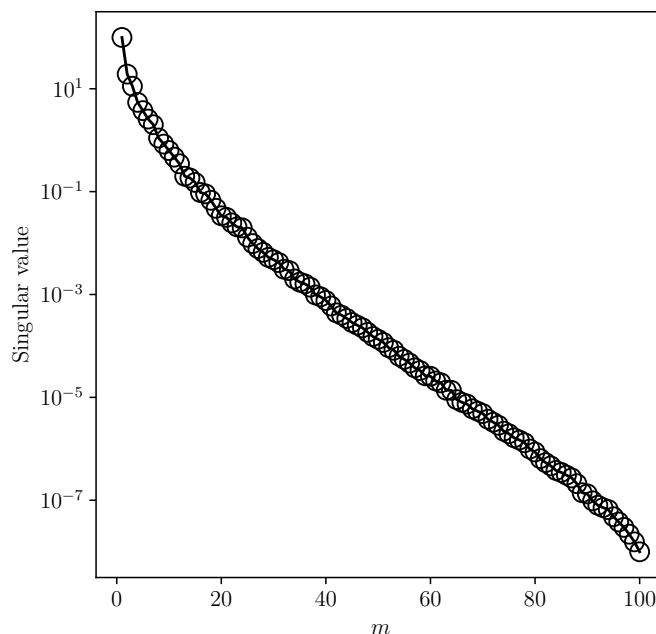


Figure 8: Singular value distribution of 100 snapshots for 2D lid-driven flow

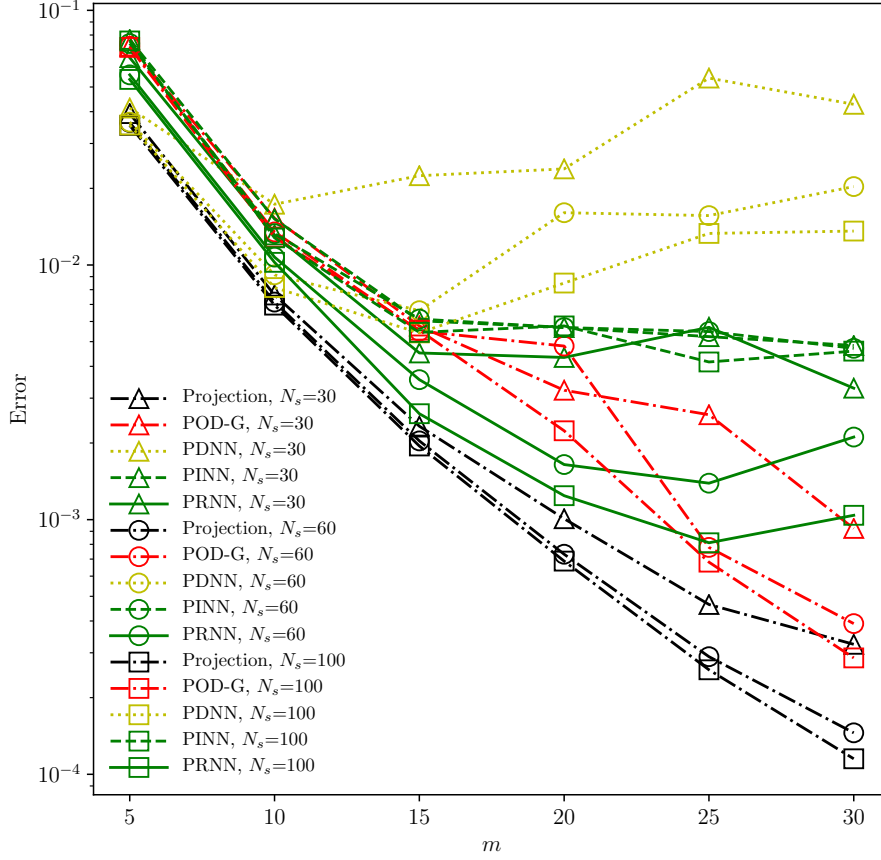


Figure 9: The prediction accuracy of the Projection, POD-G, PDNN, PINN and PRNN methods for the number of snapshots $N_s=30$, 60 and 100, respectively.

4.3. Natural convection in enclosure

To further test the prediction accuracy of the networks for more complex problems, natural convection in enclosure problem is considered. The geometry and boundary conditions are shown in Fig. 7(b). The unit square cavity is filled with incompressible Newtonian fluid. The cavity is heated and cooled differentially on the two opponent sides, with the other two sides insulated. The gravity acts in the vertical direction. The flow is driven by the vertical buoyancy force, which is modeled according to Boussinesq approximation. The cavity is deployed with a rotation angle θ . To address the variable geometry, a variable coordinate system is applied with x -axis perpendicular to the heated/cooled sides. Thus, the flow is governed by the following two-dimensional incompressible Navier-Stokes equation and energy equation:

$$\begin{aligned}
 \nabla \cdot \mathbf{u} &= 0 \\
 (\mathbf{u} \cdot \nabla) \mathbf{u} &= -\nabla p + \sqrt{\left(\frac{Pr}{Ra}\right)} \nabla^2 \mathbf{u} + T \mathbf{n}_g \\
 (\mathbf{u} \cdot \nabla) T &= \frac{1}{\sqrt{(Pr \times Ra)}} \nabla^2 T,
 \end{aligned} \tag{45}$$

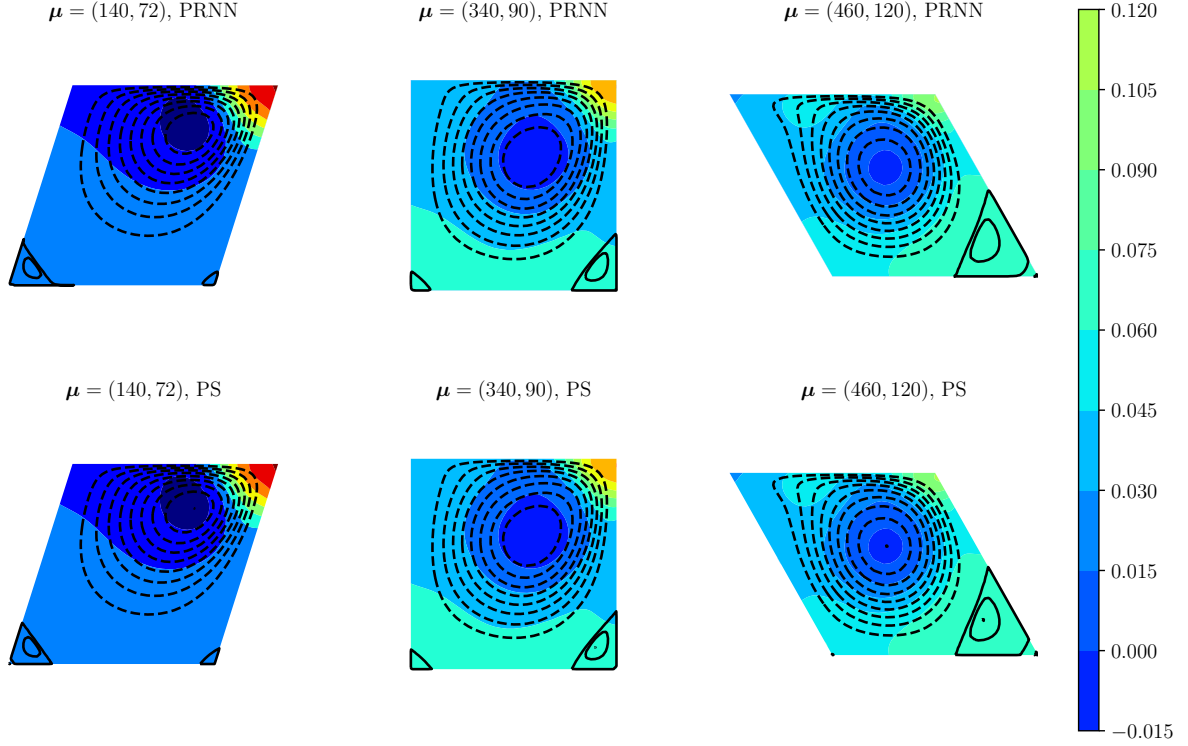


Figure 10: The comparison of pressure contour and streamlines between the Chebyshev pseudospectral (PS) and the PRNN solutions for four specific parameters. The results of the PRNN are obtained via employing the $m=25$ modes extracted from 100 snapshots and a network of $L=5$ and $n_H=30$ architecture trained with 20000 residual points. The solid streamline indicates an anticlockwise vortex, the dashed streamline an clockwise vortex.

where $\mathbf{u} = (u, v)$ is the dimensionless velocity in Cartesian coordinate $\mathbf{x} = (x, y)$, p is the pressure, ∇ is the Hamiltonian operator, Ra is the Rayleigh number, Pr is the Prandtl number, $\mathbf{n}_g = (\sin(\theta), \cos(\theta))$ is the unit vertical vector. All the sides are no-slip walls. The heated and cooled sides are enforced with the dimensionless temperature $T = 0.5$ and $T = -0.5$, respectively. The other two sides are enforced with adiabatic boundary condition $\partial T / \partial y = 0$. Similarly, the flow is solved with the Chebyshev pseudospectral method accompanied with the $IP_N - IP_{N-2}$ scheme on a grid of 49×49 .

The parameter space of interest is $\boldsymbol{\mu} = (Ra, Pr, \theta) \in [10^4, 10^5] \times [0.6, 0.8] \times [\pi/4, \pi/2]$. 200 snapshots of high-fidelity solutions for parameters generated with Sobol sequence are calculated and collected for building the reduced basis, and the corresponding singular value distribution is plotted in Fig. 11. It is shown that the singular value decays slowly, implying that more modes are required to represent the underlying dynamic. We choose $m = 5, 10, 15, \dots, 30$ modes to test the prediction accuracy of PDNN, PINN and PRNN. To test the prediction accuracy, a test data set of size $6 \times 6 \times 6 = 216$ is generated on a tensor-product parameter grid $\boldsymbol{\mu} = \{(1 + 1.8i) \times 10^4\}_{i=0}^5 \times \{0.6 + 0.04j\}_{j=0}^5 \times \{\pi/4 + k\pi/20\}_{k=0}^5$. Similarly, for testing the prediction accuracy of the POD-G method, the solving of the reduced-order model for a parameter $\boldsymbol{\mu}$ starts from the projection coefficients of the full-order solution $\phi_h(\boldsymbol{\mu})$ on the reduced basis. For comparison, we pick the first 30, 100 snapshots from the 200 snapshots to do the same test. As for the training of networks, we use the same following hyperparameters: 40000 epoches, batch size 1000, the leaning rate initialized as 0.01 and decaying by 96% every 200 epoches.

The prediction accuracy is shown in Fig. 12. The tendency of PDNN, PINN and PRNN is similar with that in Fig. ???. Both the PINN and PRNN are much better than the PDNN. Both the PINN and PRNN can achieve a higher accuracy with 30 snapshot than the PDNN even with 200 snapshots. Besides, the PRNN is the best choice, as it not only enjoys a high accuracy, but also shows an improvement with the increase of the snapshots. The further confirmation of the reliability of PRNN is shown in Fig. 13, offering a good agreement between the Chebyshev pseudospectral method and PRNN for some specific parameters. Also, the displayed streamlines are derived from solving Eq. 44.

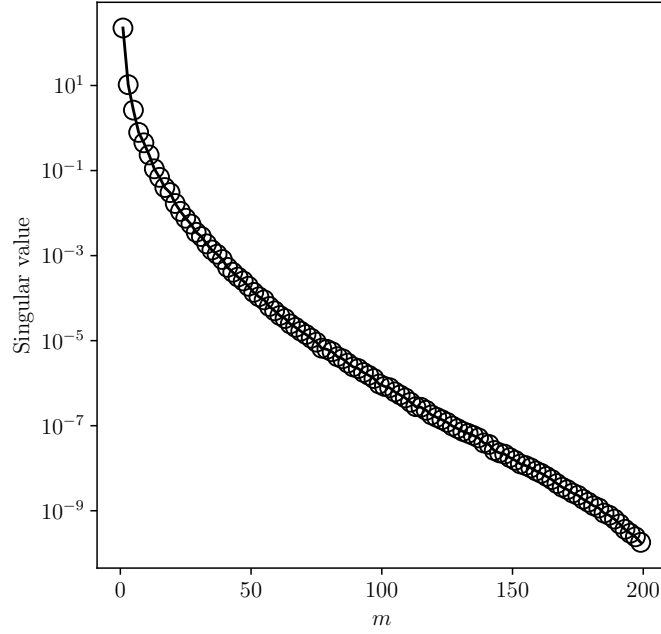


Figure 11: *Singular value distribution of 200 snapshots for 2D lid-driven flow*

5. Conclusions

Acknowledgments

The first author is financially supported by Xi'an Jiaotong University xxx.

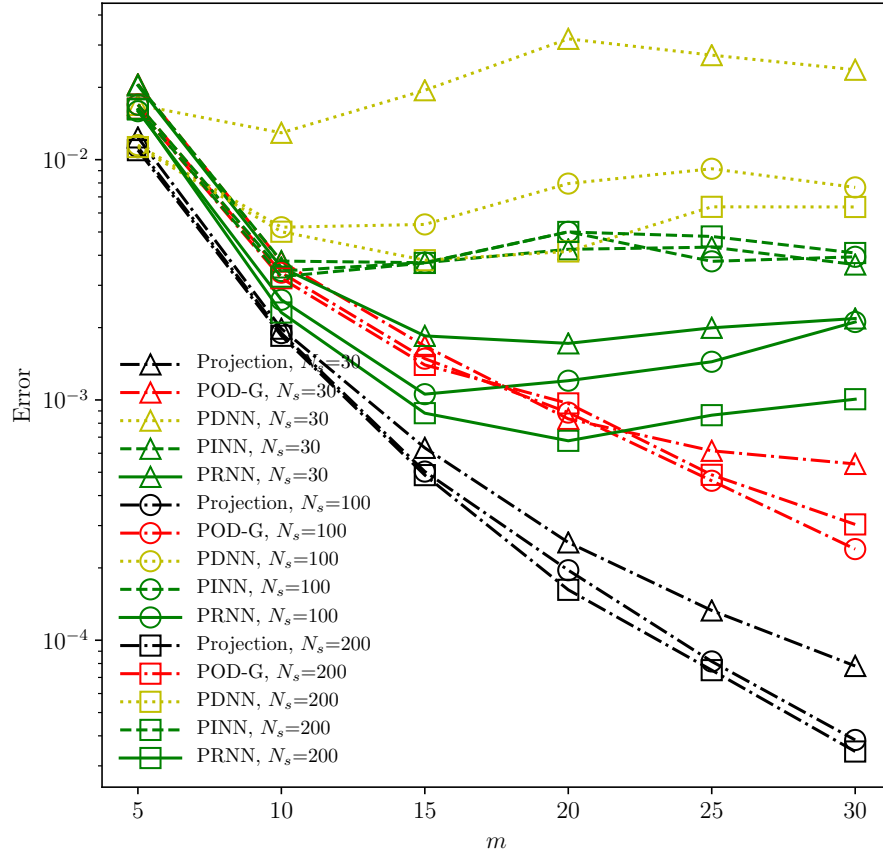


Figure 12: The prediction accuracy of the Projection, POD-G, PDNN, PINN and PRNN methods for the number of snapshots $N_s=30, 60$ and 100 , respectively.

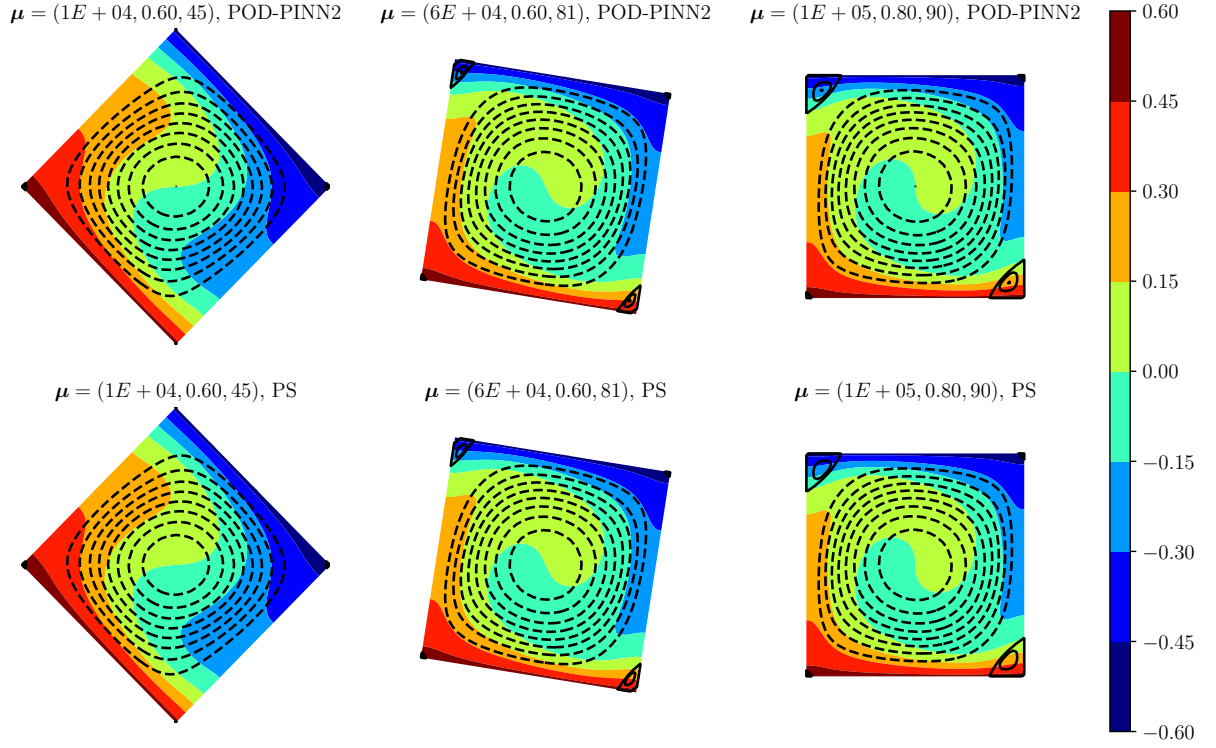


Figure 13: The comparison of pressure contour and streamlines between the Chebyshev pseudospectral (PS) and the PRNN solutions for four specific parameters. The results of the PRNN are obtained via employing the $m=25$ modes extracted from 100 snapshots and a network of $L=5$ and $n_H=30$ architecture trained with 20000 residual points. The solid streamline indicates an anticlockwise vortex, the dashed streamline an clockwise vortex.